



Near-surface heating on Enceladus and the south polar thermal anomaly

J. H. Roberts¹ and F. Nimmo¹

Received 20 February 2008; accepted 3 April 2008; published 3 May 2008.

[1] Strike-slip motion is predicted to be a consequence of diurnal tidal stresses in most satellites of the outer solar system. Such motion can lead to near-surface heating through friction or viscous dissipation. Here we discuss the effect of near-surface shear heating on convection in the underlying ice shells of icy satellites. We present models of convection in spherical shells including tidal and shear heating, and show that localized near-surface heating enhances convective upwelling beneath it. The near-surface heating promotes regional melting of the ice shell, which likely results in subsidence of the surface topography. The long-wavelength geoid resulting from the subsidence, plume buoyancy and dynamic topography may lead to small (4° per Ma) amounts of true polar wander, potentially contributing to the south polar location of the observed thermal anomaly. However compositional effects are likely required in addition to thermal effects to generate larger degrees of reorientation. **Citation:** Roberts, J. H., and F. Nimmo (2008), Near-surface heating on Enceladus and the south polar thermal anomaly, *Geophys. Res. Lett.*, 35, L09201, doi:10.1029/2008GL033725.

1. Introduction

[2] Enceladus currently exhibits a surprising level of activity for its size, particularly in the south polar region. The region south of 55° S latitude is depressed ~ 200 m [Thomas *et al.*, 2007], and is scored with four large tectonic faults informally named the “tiger stripes”, out of which flow plumes of vapor and ice crystals [Porco *et al.*, 2006]. A net heat flow of 4–7 GW has been observed for the south polar region [Spencer *et al.*, 2006]. The origin of the thermal anomaly is not well understood, but tidal dissipation is a strong candidate for the source of this heat [e.g., Ross and Schubert, 1989; Collins and Goodman, 2007].

[3] In addition to global dissipation in the icy interior, strike-slip motion is predicted to be another consequence of diurnal tidal stresses [Hoppa *et al.*, 1999], and may lead to localized near-surface heating along fracture zones through viscous dissipation or friction [Nimmo and Gaidos, 2002]. Nimmo *et al.* [2007] showed that the observed heat and vapor flux in the south polar region of Enceladus could be produced by shear heating along the “Tiger-stripe” fracture zones.

[4] The polar location of the hot spot may be the result of satellite reorientation due to the presence of a low-density diapir [Nimmo and Pappalardo, 2006]. Such a diapir might

arise due to thermal or compositional convection, or a combination of the two.

[5] Here we investigate whether the inferred near-surface shear heating could have affected underlying convection in the ice shell [cf. Han and Showman, 2008]. In particular, we examine the effect of shallow heating on melt production and dynamic topography to determine the extent to which such heating could have promoted true polar wander (TPW).

2. Modeling

[6] We computed the spatially-variable tidal heating distribution, H_{tidal} in an Enceladus model with three primary layers, a silicate core of radius 160 km, overlain by a water ocean and icy mantle with combined thickness 90 km. We allowed the ice-water interface depth to vary between models. Using the general approach of Tobie *et al.* [2005], and a propagator matrix method similar to Sabadini and Vermeersen [2004], we solved for the heating in a spherical ice shell with two viscosity layers, a lower layer with viscosity near the melting point, $\eta_0 = 3 \times 10^{13} - 10^{14}$ Pa s and a high-viscosity layer with $\eta = 10^6 \eta_0$, and a thickness calculated in an iterative fashion to be consistent with the thickness of the high-viscosity ($\eta(r) \geq 10^3 \eta_0$) region from our convection models [Roberts and Nimmo, 2008]. The liquid layer is necessary to mechanically decouple the ice shell from the silicate core; without it the tidal heating is severely reduced.

[7] For each case, we first generated a reference H_{tidal} distribution using the method outlined above, and used this as a spatially variable internal heating rate for thermal convection models of the ice shell. Free-slip and temperature boundary conditions were imposed at the top and bottom of the ice shell. The ice shell is internally heated by tidal dissipation and, potentially, by near-surface shear heating. The base of the ice shell is held at 273 K. The surface temperature, T_s varies with latitude as in work by Ojakangas and Stevenson [1989], from 75 K at the equator to 57 K at the poles. Convection is governed by the conservation equations of mass, momentum, and energy, subject to the Boussinesq approximation, and assuming incompressibility [Zhong *et al.*, 2000]. The calculations were done with Citcom [Roberts and Zhong, 2004], a finite-element code in 2D-axisymmetric geometry, using 192 elements laterally, and either 48 or 64 elements radially, depending on the thickness of the ice shell. The viscosity is Newtonian and temperature-dependent:

$$\eta(T) = A \exp\left(\frac{E_a}{R_g T}\right) \quad (1)$$

¹Department of Earth and Planetary Science, University of California, Santa Cruz, California, USA.

Table 1. Global Model Parameters

Parameter	Value
ρ_{ice}	925 kg m ⁻³
ρ_{water}	1000 kg m ⁻³
g	0.112 m s ⁻²
R_s	250 km
α	1.22×10^{-4} K ⁻¹
κ	1.97×10^{-6} m ² s ⁻¹
k	3 W m ⁻¹ K ⁻¹
L_f^a	334 kJ kg ⁻¹
ΔT	198 K
$T_{s,ca}$	75 K

^aLatent heat of fusion.

where A is a pre-exponential factor chosen such that at the base of the ice shell $\eta = \eta_0$, the reference viscosity. T is the temperature, R_g is the gas constant, and E_a is the activation energy for diffusion creep (thought to be the dominant deformation mechanism for Europa [Moore, 2006]), taken to be 60 kJ mol⁻¹ [Moore, 2006]. The tidal heating models, by necessity, assume spherically symmetric mechanical properties. Because the convection may introduce strong lateral viscosity variations, at each time step we perturb H_{tidal} for each element based on the local viscosity [see also Ojakangas and Stevenson, 1989; Sotin et al., 2002].

[8] To examine the effects of near-surface heating on the convection, in some cases we impose an additional localized heat source in the top 5 km of the ice shell. Based on the observed area of and heat flux in the Tiger-stripe region [Spencer et al., 2006], we placed a total of 7 GW of heating in the region within 35° of the south pole of the convection model, distributed in a $\cos^2\theta$ pattern, where θ is the angular distance from the pole. The combination of tidal and shear heating may heat the ice shell sufficiently that local melting may occur [cf. Sotin et al., 2002]. While true thermochemical convection models are beyond the scope of this paper, we do track the approximate local melt production rate. When the temperature of an element exceeds the melting point, we reduce the temperature to the melting point, and assume that the energy that would have heated the ice above the melting point instead goes into melting the ice. We track the melt production over time, and assume that the liquid drains rapidly into a subsurface ocean or regional sea [Collins and Goodman, 2007]. Each convection model is run until the heat flux at the top and bottom boundaries reaches steady-state.

3. Results

[9] We ran six models in which we tested the effects of shell thickness d , and near-surface shear heating H_{shear} . Cases 1–4 have $\eta_0 = 3 \times 10^{13}$ Pa s, or a Rayleigh number

$Ra = 6.6 \times 10^8$. Cases 5 and 6 have $\eta_0 = 10^{14}$ Pa s, ($Ra = 2.0 \times 10^8$). $Ra = \frac{\rho g \alpha \Delta T R_s^3}{\kappa \eta_0}$, where ρ is the density, g is the gravity, α is the thermal expansivity, ΔT is the temperature difference across the ice shell at the equator, R_s is the surface radius, and κ is the thermal diffusivity. The values of the global properties and the parameters specific to each case are listed in Tables 1 and 2 respectively.

[10] Cases 1 and 2 are identical except for the inclusion of 7 GW of H_{shear} in the south polar region of Case 2. The heating rate and temperature distributions for these two cases are shown in Figure 1. In these models convection is relatively sluggish - the stagnant lid is thick, and the upwellings are widely separated. However, even though the extra south polar heating is confined to shallow levels, it is clear that the deeper temperature structure is profoundly affected. The physical reason for these effects is relatively straightforward: a near-surface heat-generating layer flattens the temperature gradient and thus insulates the interior. The temperature fields (right panels of Figure 1) show that the stagnant lid is significantly thinned, and there is an enlarged hot spot at the South pole.

[11] We have tracked the melt production as described in the previous section, and find that 6.7×10^3 km³ (6.2×10^{15} kg) of melt is generated in 1 Ma in Case 2. The average melting rates, \dot{M} are listed for each case in Table 2. The melting is confined to a relatively small region at the poles where the tidal heating is the strongest. When shear heating is present, the melting is enhanced in the south polar region.

[12] The surface expression of shallow heating is dramatic. When shear heating is present, the dynamic topography and corresponding geoid are greatly increased in the south polar region, but largely unaffected elsewhere (Figure 2a). The variation in topography is mirrored in the elastic thickness T_e (Figure 2b), here defined as the depth to the 160 K isotherm [Nimmo et al., 2002]. $T_e = 23$ km in Case 1 and much of Case 2, but thins to 2 km directly above the south pole in Case 2. The lithosphere within 20° of the pole in Case 2 is thus much more susceptible to deformation or fracture, e.g. the tiger-stripes. The heat flow in the shear heated region is also much greater than the background (Figure 2c), although this is primarily due to the imposed shallow heating rather than the deeper convective contribution.

[13] Qualitatively, the results for Cases 3 and 4 are similar to Cases 1 and 2, respectively. However, due to the enhanced tidal heating in the thinner ice shell, melting is much more prevalent in Case 4 than in Case 2, although still confined to the south polar region. The insulating effect of

Table 2. Model-Specific Parameters^a

Case	d , km	η_0 , Pa s	H_{shear}	\dot{M} , kg y ⁻¹	$N_2^{dyn,f}$, m	\dot{h}^{sub} , $\frac{m}{My}$	\dot{N}_2^{sub} , $\frac{m}{My}$	Q	δ , deg
1	70	3×10^{13}	no	1.20×10^9	0.81	18.5	-3.45	-0.0154	-0.12
2	70	3×10^{13}	yes	6.2×10^9	-44	95.7	-17.8	-0.36	-2.85
3	40	3×10^{13}	no	8.1×10^7	10.7	1.25	-0.23	0.061	0.48
4	40	3×10^{13}	yes	1.70×10^{10}	-27	263	-49	-0.44	-3.48
5	70	10^{14}	no	0	18.4	0	0	0.107	0.85
6	70	10^{14}	yes	6.9×10^7	-33	1.07	-0.199	-0.196	-1.55

^a \dot{M} , melt rate; $N_2^{dyn,f}$, filtered dynamic geoid at $\ell = 2$; Q , load after 1 Ma melting; \dot{h}^{sub} , subsidence topography rate; \dot{N}_2^{sub} , subsidence geoid rate at $\ell = 2$; δ , TPW after 1 Ma melting.

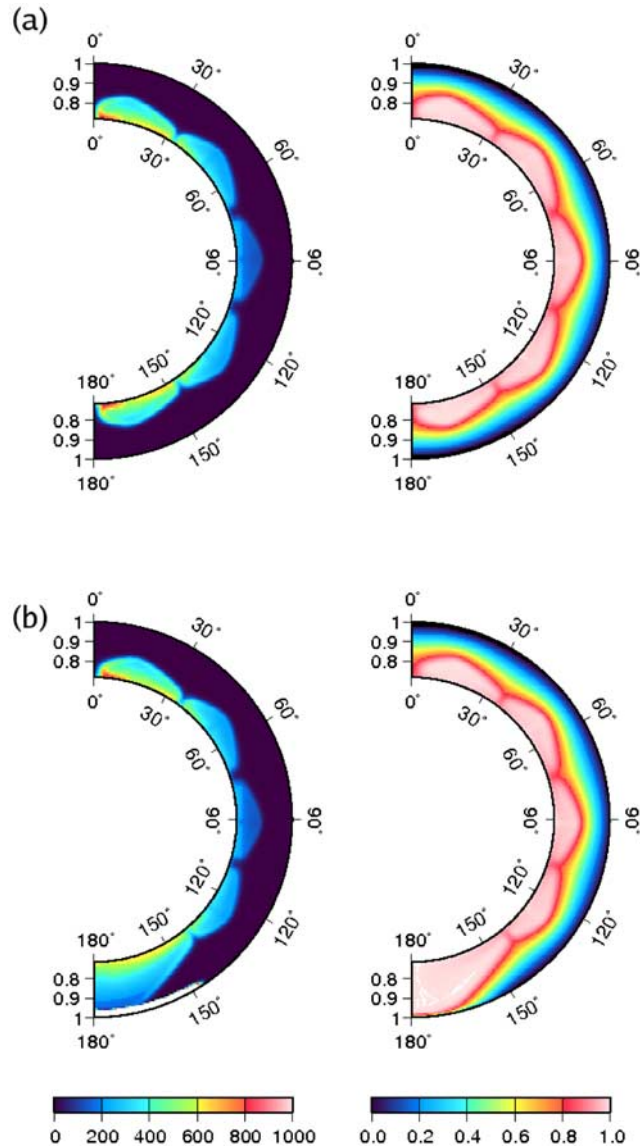


Figure 1. 2D axisymmetric convection cases with tidal dissipation: (a) Case 1, no shear heating and (b) Case 2, including a near-surface region of shear heating near the south pole. For each case the heating rate (left, scale is 10^{-9} W m^{-3}), and the nondimensional temperature T' (right) are shown. $T' = 0$ corresponds to $T = 75 \text{ K}$, and $T' = 1$ corresponds to $T = 273 \text{ K}$. Note the large temperature increase beneath the South pole in Figure 1b relative to Figure 1a.

the shear heated region is necessary to produce significant amounts of melt. Very little melt occurs in Case 3.

[14] Case 5, with higher reference viscosity, does not convect. However, in the corresponding Case 6, with near-surface heating, the temperature beneath the heated region is substantially elevated. The velocity of material in the warm south polar region is also increased, resulting in regional circulation ($v \sim 70 \text{ cm yr}^{-1}$), although the rest of the ice shell is relatively stagnant ($v \lesssim 0.5 \text{ mm yr}^{-1}$). However, very little melting occurs in this case. Because the ice viscosity is higher than in Case 2, the tidal heating is lower.

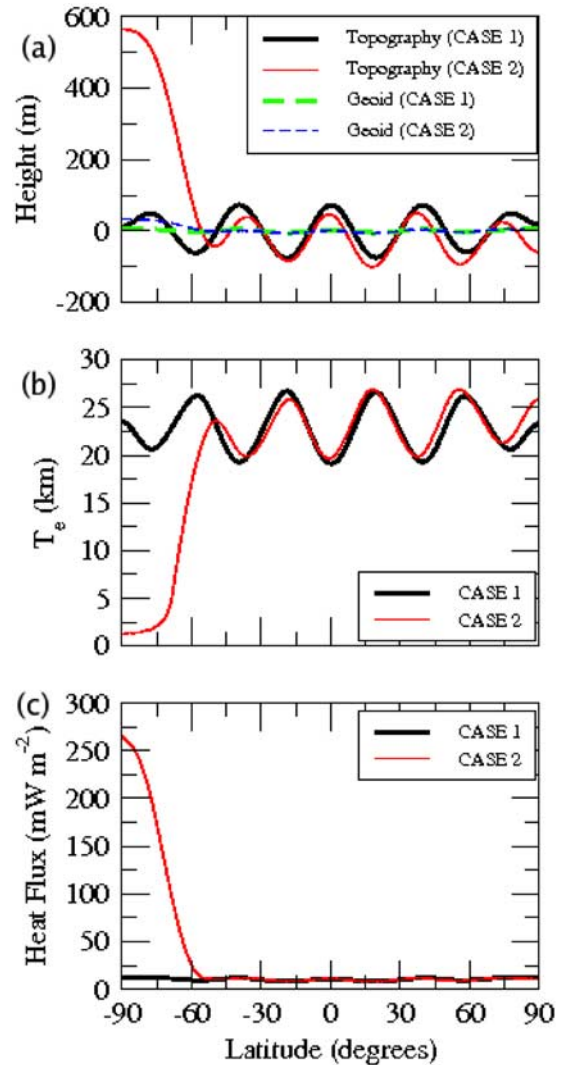


Figure 2. Latitude-dependent properties for Case 1 (thick lines) and 2 (thin lines) illustrating the effect of H_{shear} in Case 2. (a) Dynamic topography (solid) and geoid (dashed) for $\ell \leq 20$. (b) T_e measured as the depth to the 160 K isotherm. T_e for both cases averages 23 km outside the south polar terrain, but in Case 2 is 2 km near the pole. Note however, that this thin lithosphere zone is smaller in extent than the full shear zone. (c) Surface heat flux. The dramatic increase in heat flux in the polar region of Case 2 is largely an effect of the imposed shallow H_{shear} .

The deep ice does not exceed the melting point, and the melt is restricted to a region immediately below the center of the zone of shear heating.

4. Discussion

[15] Figures 1 and 2 show that near-surface heating can profoundly affect convection in the ice shell [cf. *Han and Showman, 2008*]. An enhanced upwelling develops (Figure 1b), perturbing the local geoid and topography (Figure 2a). H_{shear} produces a locally thinned lithosphere above the buoyant material, allowing the upwelling to rise to a shallower depth (Figure 2b).

[16] A possible result of such an upwelling diapir is planetary reorientation [Nimmo and Pappalardo, 2006]. TPW is driven by the $\ell = 2$ component of mass anomalies. In this model, the principal mass anomalies are due to the topography at the surface and base of the ice shell, and the buoyancy of the upwelling plume.

[17] For example, Case 2, with a strong upwelling beneath a region of shear heating shows a strong $\ell = 2$ component of dynamic topography, h^{dyn} at the surface of 174 m. The h^{dyn} is an expression of buoyant upwellings in the deep ice shell and the warm shear-heated region in the near surface. The buoyant material is a mass deficit, and has a negative geoid at $\ell = 2$, largely counteracting the topographic contribution. Thus, the net dynamic geoid at $\ell = 2$, N_2^{dyn} is only 15.2 m, assuming an isostatic response to the internal load. The presence of an elastic lithosphere, however, will reduce h^{dyn} . In this case the resulting dynamic geoid, $N_2^{dyn,f}$ will be dominated by the plume buoyancy and thus be negative [Roberts and Zhong, 2004; Nimmo and Pappalardo, 2006]. We therefore apply an elastic filter [Turcotte et al., 1981; Roberts and Zhong, 2004] to the surface topography to account for the elastic effect. We find that for $T_e = 23$ km, rigidity of 4 GPa, and a Poisson ratio of $\frac{1}{3}$, the degree of compensation at $\ell = 2$ [Turcotte et al., 1981] is only 1.9%. h_2^{dyn} for Case 2 is reduced to 3.4 m, and $N_2^{dyn,f} = -44$ m. $N_2^{dyn,f}$ for all cases is given in Table 2, after elastic filtering where $T_e = 23$ km for the thick-shell cases and $T_e = 18.5$ km for the thin-shell cases.

[18] Additional geoid anomalies may arise from melting of the ice shell. The volume change associated with the melting of ice I will result in topographic subsidence above the melt region [Collins and Goodman, 2007]. This scenario is consistent with the observation that the tiger-stripe region lies in a topographic depression [Thomas et al., 2007].

[19] In the example of Case 2, 6.7×10^3 km³ of ice melts in 1 Ma. If the ice shell responds isostatically to the removal of material, the net volume decreases by 500 km³. Distributed over the areal extent of the Tiger-stripe region (roughly 7×10^4 km² [Porco et al., 2006]), the corresponding subsidence topography, h^{sub} is 7.2 m. This, however is a minimum estimate. If the melt drains into a subsurface ocean, and the base of the ice shell stays flat (e.g., due to lateral flow of ice), then the subsidence volume will be equal to the total volume of melted ice. Because the surface ice is cold and rigid, it can likely support this larger amount of topography rather than responding isostatically. The ice melted in 1 Ma in Case 2 would thus result in $h_{sub} = 96$ m. This is equivalent to 51 m at $\ell = 2$ and produces an $\ell = 2$ geoid of $N_2^{sub} = -17.8$ m. Case 4, the thin-shell counterpart to Case 2 is more productive, and results in $h^{sub} = 263$ m and $N_2^{sub} = -49$ m after 1 Ma. The maximum rates of growth of h^{sub} and N_2^{sub} for all cases (assuming the base of the ice shell remains flat) are given in Table 2. The total degree-2 geoid N_2 is the sum of the filtered dynamic geoid and the geoid due to subsidence over a time Δt : $N_2 = N_2^{dyn,f} + N_2^{sub} \Delta t$.

[20] TPW is driven by this N_2 , but is opposed by the fossil portions of the rotational and tidal bulges. The fossil bulge is a function of the lithospheric strength, characterized by the tidal Love number, k_2^T . A load will result in TPW of

$\delta = \frac{1}{2} \sin^{-1}[Q \sin(2\theta^f)]$ [Matsuyama and Nimmo, 2007], where θ^f is the final co-latitude of the load, and Q is a nondimensional parameter describing the size of the geoid anomaly N_2 relative to the fossil bulge [Willemann, 1984]:

$$Q = \frac{3\sqrt{5}gN_2}{(R_s\Omega)^2(k_2^{T*} - k_2^T)} \quad (2)$$

where Ω is the rotational frequency, and k_2^{T*} is the Love number in the fluid limit. If $|Q| > 1$, the load exceeds the rotational bulge and can drive significant TPW [Matsuyama et al., 2006]. k_2^T for our tidal heating models is 5.0×10^{-3} and 10.7×10^{-3} for the thick- and thin-shell models respectively, compared with ~ 0.75 for a fluid Enceladus. Combining $N_2^{dyn,f}$ with the $\ell = 2$ geoid resulting from 1 Ma of melting and subsidence, we obtain $Q = -0.36$ for Case 2.

[21] A negative Q indicates poleward migration of the load. The actual separation of the pole and the center of the tiger-stripe region may be as much as 8° [Matsuyama and Nimmo, 2007]. If the shear zone initially formed off the rotation axis, up to 2.85° of poleward TPW would be possible in Case 2 after 1 Ma of melting. Cumulative melting over a greater time span could increase the subsidence and the geoid. In order to attain $|Q| > 1$ in Case 2, 7.2 Ma of sustained melting is required, which is consistent with the surface age of the south polar terrain [Porco et al., 2006]. However, this duration of melting also results in $h_{sub} = 0.65$ km, which is not supported by observation [Thomas et al., 2007]. Q and δ for all cases is given in Table 2, assuming 1 Ma of melt production and $\theta^f = 8^\circ$. In no case does the calculated TPW exceed 4° ; longer melt durations would result in greater subsidence and more reorientation. If the ice shell in the south polar region responded isostatically to the melting, similar amounts of h_{sub} would be required to get the same Q , but would simply take a factor of $\rho_{ice}/(\rho_{water} - \rho_{ice})$ longer.

5. Conclusions

[22] Near-surface shear heating such as that observed at Enceladus perturbs the underlying convection and results in enhanced upwelling, melt generation, and a thinned lid. The geoid due to melt-related subsidence and locally elevated temperatures may drive small amounts of TPW. However, additional physics and chemistry not considered here may be important. For example, partial melting of the upwelling ice shell will remove impurities, resulting in a greater density difference between the “clean” ice in the diapir, and the “dirty” ice in the surroundings, than by temperature variations alone [Pappalardo and Barr, 2004]. Such an enhanced density contrast may increase the size of the internal load and promote TPW. The effects of chemistry and the inclusion of impact-related heat are topics for future work in this area. These models can also be improved by using a full 3D geometry. This is presently computationally expensive, but is the next obvious step.

[23] **Acknowledgments.** The authors would like to thank two anonymous reviewers for their helpful comments. This research is supported by NASA grant NNX07AL30G.

References

- Collins, G. C., and J. C. Goodman (2007), Enceladus' south polar sea, *Icarus*, *189*, 72–82, doi:10.1016/j.icarus.2007.01.010.
- Han, L., and A. P. Showman (2008), Implications of shear heating and fracture zones for ridge formation on Europa, *Geophys. Res. Lett.*, *35*, L03202, doi:10.1029/2007GL031957.
- Hoppa, G., B. R. Tufts, R. Greenberg, and P. Geissler (1999), Strike-slip faults on Europa: Global shear patterns driven by tidal stress, *Icarus*, *141*, 287–298, doi:10.1006/icar.1999.6185.
- Matsuyama, I., and F. Nimmo (2007), Rotational stability of tidally deformed planetary bodies, *J. Geophys. Res.*, *112*, E11003, doi:10.1029/2007JE002942.
- Matsuyama, I., J. X. Mitrovica, M. Manga, J. T. Perron, and M. A. Richards (2006), Rotational stability of dynamic planets with elastic lithospheres, *J. Geophys. Res.*, *111*, E02003, doi:10.1029/2005JE002447.
- Moore, W. B. (2006), Thermal equilibrium in Europa's ice shell, *Icarus*, *180*, 141–146, doi:10.1016/j.icarus.2005.09.005.
- Nimmo, F., and E. Gaidos (2002a), Strike-slip motion and double ridge formation on Europa, *J. Geophys. Res.*, *107*(E4), 5021, doi:10.1029/2000JE001476.
- Nimmo, F., and R. T. Pappalardo (2006), Diapir-induced reorientation of Saturn's moon Enceladus, *Nature*, *441*, 614–616, doi:10.1038/nature04821.
- Nimmo, F., R. T. Pappalardo, and B. Giese (2002b), Effective elastic thickness and heat flux estimates on Ganymede, *Geophys. Res. Lett.*, *29*(7), 1158, doi:10.1029/2001GL013976.
- Nimmo, F., J. R. Spencer, R. T. Pappalardo, and M. E. Mullen (2007), Shear heating as the origin of the plumes and heat flux on Enceladus, *Nature*, *447*, 289–291, doi:10.1038/nature05783.
- Ojakangas, G. W., and D. J. Stevenson (1989), Thermal state of an ice shell on Europa, *Icarus*, *81*, 220–241, doi:10.1016/0019-1035(89)90052-3.
- Pappalardo, R. T., and A. C. Barr (2004), The origin of domes on Europa: The role of thermally induced compositional diapirism, *Geophys. Res. Lett.*, *31*, L01701, doi:10.1029/2003GL019202.
- Porco, C. C., et al. (2006), Cassini observes the active south pole of Enceladus, *Science*, *311*, 1393–1401, doi:10.1126/science.1123013.
- Roberts, J. H., and F. Nimmo (2008), Tidal heating and the long-term stability of a subsurface ocean on Enceladus, *Icarus*, *194*, 675–689, doi:10.1016/j.icarus.2007.11.010.
- Roberts, J. H., and S. Zhong (2004), Plume-induced topography and geoid anomalies and their implications for the Tharsis rise on Mars, *J. Geophys. Res.*, *109*, E03009, doi:10.1029/2003JE002226.
- Ross, M. N., and G. Schubert (1989), Viscoelastic models of tidal heating in Enceladus, *Icarus*, *78*, 90–101, doi:10.1016/0019-1035(89)90071-7.
- Sabadini, R., and B. Vermeersen (2004), *Global Dynamics of the Earth: Applications of Normal Mode Relaxation Theory to Solid-Earth Geophysics*, Kluwer Acad., Dordrecht, Netherlands.
- Sotin, C., J. W. Head III, and G. Tobie (2002), Europa: Tidal heating of upwelling thermal plumes and the origin of lenticulae and chaos melting, *Geophys. Res. Lett.*, *29*(8), 1233, doi:10.1029/2001GL013844.
- Spencer, J. R., et al. (2006), Cassini encounters Enceladus: Background and the discovery of a south polar hot spot, *Science*, *311*, 1401–1405, doi:10.1126/science.1121661.
- Thomas, P. C., et al. (2007), Shapes of the Saturnian icy satellites and their significance, *Icarus*, *190*, 573–584, doi:10.1016/j.icarus.2007.03.012.
- Tobie, G., A. Mocquet, and C. Sotin (2005), Tidal dissipation within large icy satellites: Applications to Europa and Titan, *Icarus*, *177*, 534–549, doi:10.1016/j.icarus.2005.04.006.
- Turcotte, D. L., R. J. Willemann, W. F. Haxby, and J. Norberry (1981), Role of membrane stresses in the support of planetary topography, *J. Geophys. Res.*, *86*, 3951–3959.
- Willemann, R. J. (1984), Reorientation of planets with elastic lithospheres, *Icarus*, *60*, 701–709, doi:10.1016/0019-1035(84)90174-X.
- Zhong, S., M. T. Zuber, L. Moresi, and M. Gurnis (2000), Role of temperature-dependent viscosity and surface plates in spherical shell models of mantle convection, *J. Geophys. Res.*, *105*, 11,063–11,082.

F. Nimmo and J. H. Roberts, Department of Earth and Planetary Sciences, University of California, 1156 High Street, Santa Cruz, CA 95064-1077, USA. (jhr@ucsc.edu)